Chemistry – A European Journal

ChemEurJ Chemistry Europe European Chemical Societies Publishing

RESEARCH ARTICLE

Graphene-Oxide-Mediated Photothermal Ring-Closing Metathesis: A Gateway for Organelle Imaging Probes

Preeti | Ram Sewak | Tripti Mishra | Asima Sahu | Pratim Saha | Anirban Mondal | Sudipta Basu

Department of Chemistry, Indian Institute of Technology (IIT) Gandhinagar, Gandhinagar, Gujarat, India

Correspondence: Anirban Mondal (amondal@iitgn.ac.in) | Sudipta Basu (Sudipta.basu@iitgn.ac.in)

Received: 25 September 2025 | **Revised:** 20 January 2026 | **Accepted:** 23 January 2026

Keywords: fluorescent probes | graphene-oxide | organelle imaging | photothermal effect | ring-closing metathesis

ABSTRACT

Photothermal effect using mild light irradiation has emerged as an interesting strategy in modern synthetic chemistry due to its rapid reaction with high selectivity and spatiotemporal control over conventional heating. However, applying photothermal conversion to carry out organic reactions efficiently using carbon nanomaterials remained largely uncharted. To address this, herein, we report for the first time, graphene oxide (GO) as the photothermal agent to perform ring-closing metathesis (RCM) under 940 nm NIR LED light, as well as solar simulator and natural sunlight, using Grubbs-II catalyst to rapidly synthesize dihydro-pyrroles in high yield with excellent GO recyclability. Theoretical calculation unveiled that this photothermal RCM efficiency originated from the cumulative synergy between substrate-GO absorption energy, activation barrier, and nonradiative relaxation rate which emerged as the predominant contributor for the overall reaction outcome. The RCM product can be further functionalized through Pd-catalyzed Heck coupling to forge various fluorophores for efficient imaging of endoplasmic reticulum (ER), mitochondria, and Golgi apparatus (GA) in HCT-116 colon cancer cells. This GO-mediated photothermal RCM can open a new direction toward synthesizing complex organic molecules with ease and high yield for biomedical applications.

1 | Introduction

Photothermal effect, a phenomenon where nanomaterials and chromophores convert light to thermal energy by nonradiative decay through releasing nanoparticle surface localized heat [1–8]. This photothermal effect has revolutionized modern synthetic approaches to form complex molecules using mild light irradiation due to its spatial and temporal controls, improved reaction rate with high selectivity, and less by-product formation compared to the traditional bulk heating [9–13]. Despite having a wide array of available photo-sensitive materials, photothermal conversion is extensively explored in inorganic materials and biomedical applications, and currently in its infancy in organic synthesis [14–20].

Carbon nanomaterials with 1D to 3D nanostructures have emerged as interesting classes of photothermal materials due to the abundance of loosely bound π electrons, which can be irradiated to the energetically similar π^* orbitals by light irradiation, which can trigger rapid internal conversion and intersystem crossing, leading to intense localized nanoscale heating through bond vibration and rotation [21–28]. Recently, Stache et al. used carbon black (CB) as the photothermal agent for Newman-Kwart Rearrangement (NKR) as well as recycling post-consumer waste polystyrene [29, 30]. In this context, 2D-graphene-oxide (GO) has been extensively used for photothermal therapy (PTT) in biomedical applications [31–33]. Despite being readily available and inexpensive, to the best of our knowledge, GO has never been explored as the photothermal material for organic transformation.

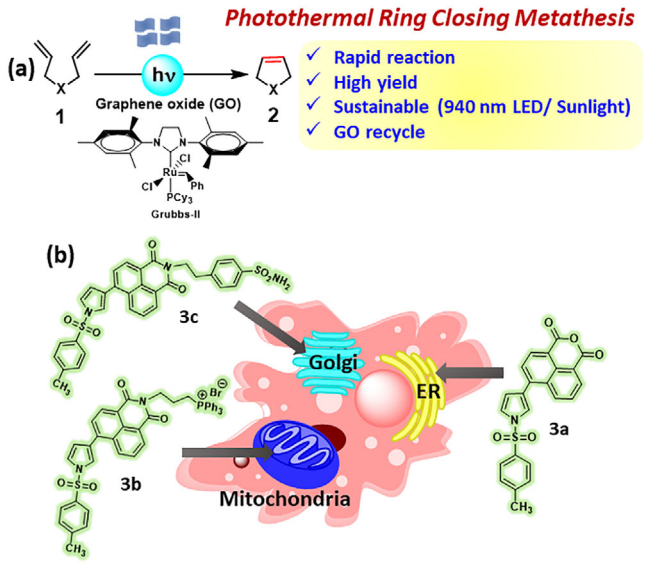

FIGURE 1 | (a) GO-mediated photothermal ring-closing metathesis (RCM). (b) Schematic representation of the synthetic fluorophores for imaging ER, mitochondria, and GA in HCT-116 colon cancer cells. ER, endoplasmic reticulum; GA, golgi apparatus; GO, graphene-oxide.

To address this, herein, we have used GO as photothermal agent to perform ring-closing metathesis (RCM) on N,N-diallyl-benzenesulfonamides under 940 nm LED light (0.15 W/cm^2), as well as under solar simulator and natural sunlight in DMF/water (1:3) using the second-generation Grubbs' catalyst (3 mol%) to afford 2,5-dihydro-pyrroles in high yield within 10 min (Figure 1a) compared to the traditional heating, with excellent GO recycling for at least six cycles. Theoretical calculations divulged that the nonradiative relaxation rate (k_{nr}), along with substrate-GO absorbance energy and activation barrier, contributed to the efficiency of the RCM outcome. The 1-tosyl-2,5-dihydro-pyrrole (2a) was further functionalized with 4-bromo-1,8-naphthalic anhydride and substituted 4-bromo-1,8-naphthalimides through Pd-catalyzed Heck coupling to obtain N-tosyl-pyrrole-naphthalimide fluorophores for imaging endoplasmic reticulum (ER), mitochondria, and Golgi apparatus (GA) in HCT-116 colon cancer cells (Figure 1b). To the best of our knowledge, this is the first example of GO-mediated photothermal RCM toward efficient synthesis of organelle imaging fluorescent probes, which opened a novel avenue for photothermal conversion in organic synthesis toward valuable materials for biomedical applications.

2 | Results and Discussion

We hypothesized that the photothermal effect of GO could be utilized to perform RCM due to its unique ability to construct C═C double bond containing carba- and hetro-cyclic rings for the total synthesis of natural products as well as unnatural complex organic molecules by using Ru-based carbene catalysts [34, 35]. RCM reactions are mostly carried out at higher bulk temperature, which might lead to the polymerization and degradation of the starting materials and products, leading to reduced reproducibility and yield. Hence, we intended to explore the localized heat generation on the GO surface under light irradiation to perform RCM with improved efficiency and sustainability. Recently,

TABLE 1 | Evaluation of the optimal condition for the photothermal effect of GO.

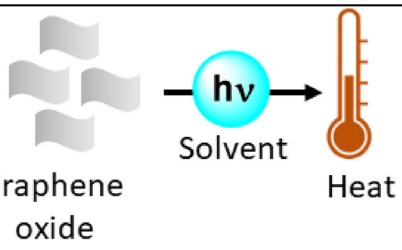

Entry	LED (nm)	Solvent	Go loading (mg/mL)	Temperature (°C)
1	445	H_2O	2	57
2	740	H_2O	2	56
3	740	H_2O	3	55
4	740	H_2O	4	53
5	940	H_2O	0.25	41.6
6	940	H_2O	0.5	45.8
7	940	H_2O	1	51.2
8	940	H_2O	2	55
9	940	Acetonitrile: H_2O (2:1)	1.5	60.4
10	940	DMF: H_2O (3:1)	1.5	60.6
11	940	DMF: H_2O (1:3)	1.5	55.1
12	940	acetone: H_2O (2:1)	1.5	55.6
13	940	DMF: H_2O (1:3)	0	39

Stache et al. reported a highly efficient method for NKR using CB as the photothermal agent with high yield under 6K white LEDs. However, (a) recyclability of CB and (b) use of lower energy near infrared (NIR) light remained majorly unaddressed [29]. Herein, we intended to use lower energy NIR LEDs/natural sunlight along with the recycling of GO for improved sustainability. First, we optimized the photothermal effect of GO under different light sources, solvents, and GO loading. GO was suspended in water and irradiated under 445, 740, and 940 nm LEDs for 20 min with different GO loading and estimated the heat generation (entries 1–8, Table 1). Interestingly, GO demonstrated heat generation till 57°C under 445 nm LED with 2 mg/mL GO loading within 20 min (entry 1, Table 1). On the other hand, under 740 nm LED, GO generated 56°C at 2 mg/mL GO loading (entry 2, Table 1). However, under 740 nm LED irradiation, GO was produced only 55°C temperature at 3 mg/mL GO loading within 20 min (entry 3, Table 1). Changing the GO loading under 940 nm LED irradiation also did not increase the temperature beyond 55°C (entries 4–8, Table 1). Based on this observation, we have chosen 940 nm LED for further optimization due to its irradiation capability into the NIR region with mild reaction conditions. We further optimized the solvent system for the metathesis reaction, having DMF/water and acetonitrile/water in different ratios under 940 nm LED irradiation for 20 min with 1.5 mg/mL GO loading (entries 9–12, Table 1). We found that GO produced 60°C temperature in acetonitrile/water (2:1) and DMF/water (3:1) in

20 min (entries 9 and 10, Table 1). On the other hand, GO exhibited 55°C temperature in DMF/water (1:3) and acetone/water (2:1), having 1.5 mg/mL GO loading within 20 min (entries 11 and 12, Table 1). We anticipate that the higher photothermal effect of GO in acetonitrile/water (3:1) and DMF/water (3:1) compared to DMF/water (1:3) was due to the better solubility of GO in organic solvents like acetonitrile and DMF compared to water to produce a more homogeneous reaction mixture. As a control experiment, without any GO, the DMF/water (1:3) mixture only generated 39°C temperature under 940 nm LED irradiation for 20 min (entry 13, Table 1). From this optimization, we have chosen DMF/water (1:3) solvent system for the photothermal effect of GO with 1.5 mg/mL loading under 940 nm LED irradiation due to its improved environment friendly approach. We also assessed the time-dependent temperature change of GO in DMF/water (1:3) under 940 nm LED for 20 min, which revealed that at 20 min, GO raised the temperature from 26°C to 55.1°C (Figure S1a). We further checked the photostability of GO under 940 nm LED, which showed that GO is extremely photo-stable for at least 3 on/off cycles of LED (Figure S1b). These optimization studies confirmed that GO (1.5 mg/mL loading) can generate the photothermal effect upon irradiation under 940 nm LED in DMF/water (1:3) within 20 min to increase the temperature to 55°C.

Encouraged by the photothermal effect of GO, we now embarked on optimizing the RCM reaction. We dissolved N,N-diallyl-4-methyl-benzene sulfonamide (1a) with Grubbs' second-generation catalyst (3 mol%) in DMF/water (1:3) and irradiated the reaction mixture under 940 nm LED in the presence of GO (1.5 mg/mL) to obtain 1-tosyl-2,5-dihydro-1H-pyrrole (2a) (Table 2, Figure S2–S4) [36]. When the reaction was carried out without any light irradiation and without any GO at 25°C and 55°C bulk heating (entries 1 and 2, Table 2), compound 2a was formed in 65% yield after 36 and 12 h, respectively. Interestingly, when we irradiated the reaction mixture under 940 nm LED for 20 min in the presence of 1.5 mg/mL GO, we obtained only 36% yield of 2a (entry 3, Table 2). A similar yield (32%) was also afforded, even reducing the time of irradiation to 12 min (entry 4, Table 2). We anticipated that under 940 nm LED irradiation at 20 min/12 min with GO (1.5 mg/mL) was generating enough surface heat to decompose the product. Hence, we carried out the reaction under 940 nm LED irradiation for 12 min as well as 10 min with the lower GO concentration of 0.75 mg/mL, which increased the yield of 2a remarkably to 81% yield (entries 5 and 6, Table 2). However, the yield of compound 2a was significantly reduced to 45% after irradiating the reaction mixture for 5 min under 940 nm LED with 0.75 mg/mL GO loading (entry 7, Table 2). We further checked the time-dependent photothermal effect of GO (0.75 mg/mL) under 940 nm LED irradiation, which exhibited that GO increased the temperature till 46°C at 20 min (Figure S1a) with excellent photostability until 3 on/off cycles (Figure S1c). We further ensured the observed photothermal effect of GO was attributed to the local temperature of the GO surface by an infrared thermal imaging camera. It was clearly observed that without and with GO (0.75 mg/mL) in DMF/water (1:3) mixture under 940 nm LED irradiation for 20 min, the local temperature of the GO surface was increased significantly from 35.2°C to 46.7°C, which confirmed that the photothermal heating generated the observed temperature at the GO surface (Figure S1d).

TABLE 2 | Evaluation of the optimal condition for the GO-mediated photothermal RCM.

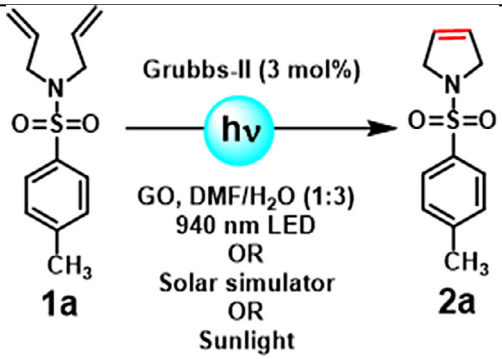

Entry[a]	LED (nm)	GO (mg/mL)	Time	Temp (°C)	Yield[b] (%)
1	No	No	36 h	25	65
2	No	No	12 h	55	65
3	940	1.5	20 min	55	36
4	940	1.5	12 min	55	32
5	940	0.75	12 min	46	81
6	940	0.75	10 min	46	81
7	940	0.75	5 min	40	45
8	No	No	10 min	46	19
9	Solar simulator	0.75	10 min	46	89
10	Sun light	0.75	3 h	46	87
11	445	0.75	10 min	45	54
12	740	0.75	10 min	46	36

[a]Reaction conditions: 1a (0.2 mmol) and Grubbs-II (3 mol%) catalyst were dissolved in DMF/water (1:3), followed by irradiation under 940 nm LED or solar simulator or natural sunlight.

[b]Yields were calculated based on the isolated products from the column chromatography as an average of three independent experiments.

To understand the effect of light and GO, we also carried out the RCM without GO and LED irradiation for 10 min under 46°C traditional heating, which yielded compound 2a with an inferior 19% yield (Entry 8, Table 2). Encouraged by this result, we carried out the GO-mediated RCM reaction under the irradiation of a solar simulator for 10 min with GO (0.75 mg/mL), which produced compound 2a with a remarkable 89% yield (entry 9, Table 2). We further irradiated the reaction mixture under natural sunlight for 3 h with GO (0.75 mg/mL), which afforded compound 2a with 87% yield (entry 10, Table 2). We anticipate that this increased time to afford 87% yield of compound 2a under natural sunlight was due to the variability of the natural sunlight intensity based on the location, time of the day, as well as time of the year. We also irradiated the reaction mixture under a higher energy light source (445 and 740 nm) for 10 min with GO (0.75 mg/mL), which afforded compound 2a with only 54% and 36% yield, respectively (entries 11 and 12, Table 2). These optimization assays clearly confirmed that RCM reaction can be carried out under 940 nm LED, solar simulator, as well as natural sunlight, with 0.75 mg/mL GO loading in the presence of Grubbs-II catalyst (3 mol %) efficiently within 10 min with

TABLE 3 | Substrate scope.

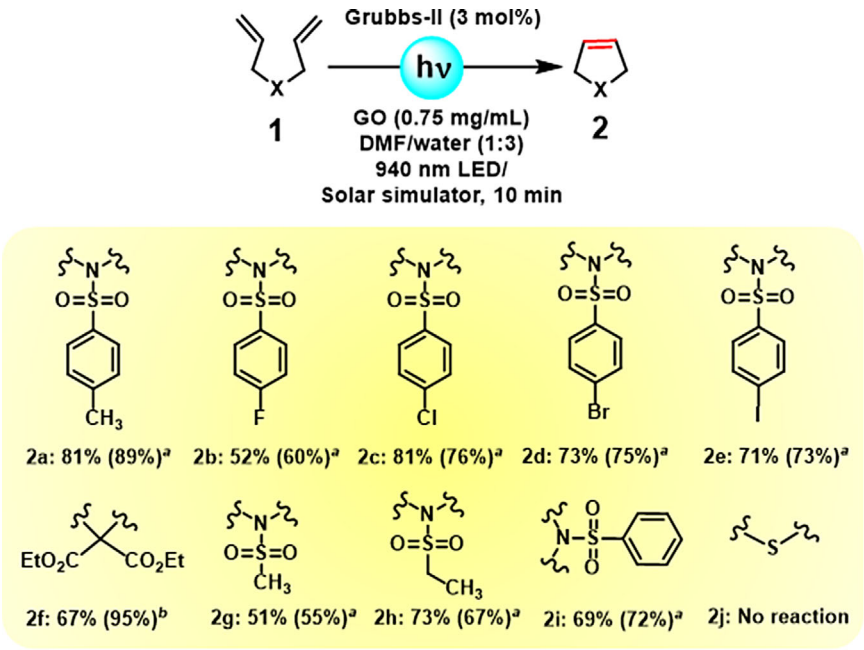

[a]The yield in the parenthesis is reported as isolated yield under solar simulator based on the average of three independent experiments.
[b]The yield was determined from the NMR experiment based on three independent experiments.

excellent yield. To understand the degree of oxidation in GO, we calculated the C:O ratio in GO before and after the RCM by x-ray photoelectron spectroscopy (XPS). The XPS data revealed that the C:O ratio was 0.89 and 1.69 before and after the reaction, indicating partial reduction during photothermal irradiation (Figure S5a). To further understand if the partial reduction of GO could change the efficiency of reaction yield, we performed photothermal RCM on compound 1a for multiple cycles using the isolated GO in the previous reaction under a solar simulator for 10 min to afford compound 2a. Surprisingly, we observed a marginal change in the yield from 89% to 83% even after six cycles. These observations clearly confirmed that the degree of oxidation in GO did not change the efficiency of the reaction yield (Figure S5b).

We further assessed the substrate scope of the light-induced GO-mediated photothermal RCM. We first varied the 4-substituents on the phenylsulfonamide ring from -F, -Cl, -Br, and -I under a 940 nm LED and solar simulator for 10 min (Figure S6, Table 3). We observed that the highest yield was found in 4-Cl-phenylsulfonamide (2c) with 81% and 76% yield under 940 nm LED and solar simulator, respectively. Alternatively, 4-F, 4-Br, and 4-I substituted compounds (2b, 2d, and 2e) were afforded in 52%, 73%, and 71% yield under 940 nm LED and 60%, 75%, and 73% yield under solar simulator, respectively (Figure S7–S15). On the other hand, compound 2f was obtained in 67% and 95% yield under 940 nm LED and solar simulator, respectively, at 10 min (Table 3 and Figures S16 and S17). We also varied the substrate for RCM by methanesulfonamide (1g), ethanesulfonamide (1h) and phenylsulfonamide (1i) (Figure S6, Table 3) which provided 2g, 2h, and 2i with 51%, 73%, and 69% yield, respectively under 940 nm LED irradiation along with 55%, 67%, and 72% yield, respectively under solar simulator irradiation for 10 min (Table 3 and Figures S18–S23). Interestingly, diallylsulfane (1j, Figure S6, Table 3) failed to produce any RCM product, which might be due to the Grubbs' second-generation catalyst poisoning by sulfur compounds.

To investigate the photothermal RCM of 1a-1e (Figure S6) on the GO surface, we employed a finite cluster model consisting of a sufficiently large graphene flake functionalized with oxygen-containing groups (epoxy and hydroxyl). The square-shaped flake with zigzag edges was passivated with hydrogen atoms, as illustrated in Figure 2a. Geometry optimizations for the adsorption complexes and the isolated species were carried out using the ORCA v.6.0.0 package [37, 38] within the density functional theory (DFT) framework. The reaction efficiency of 1a–1e complexes adsorbed on GO was determined by a delicate balance of adsorption strength, reaction barrier, and nonradiative relaxation. Among these, adsorption energy (ΔE_{ads}) plays a key role in governing surface residence time and, consequently, the extent of heat absorption. Stronger adsorption enhances the likelihood of product formation by ensuring that the reactants remain anchored on the surface long enough to undergo the necessary transformation. Our calculations show that 1e and 1a exhibited the strongest (-31.07 kcal mol^{-1}) and the weakest (-26.82 kcal mol^{-1}) adsorption, respectively (Table S1). Reaction kinetics were further dictated by the activation barrier (E_{act}) for the conversion of open-chain (1a-1e) (Figure S6) to closed-chain (2a–e) species on GO. A lower barrier facilitates the progression of the catalytic pathway, while a higher barriers impose kinetic limitations. The lowest E_{act} was obtained for 1c (169.86 kcal mol^{-1}), whereas the highest barrier corresponded to 1a (299.90 kcal mol^{-1}), highlighting the variability in reactivity across the substituents (Table S1).

Since the underlying mechanism is predominantly photothermal, the k_{nr} emerges as a crucial descriptor. With its manifold

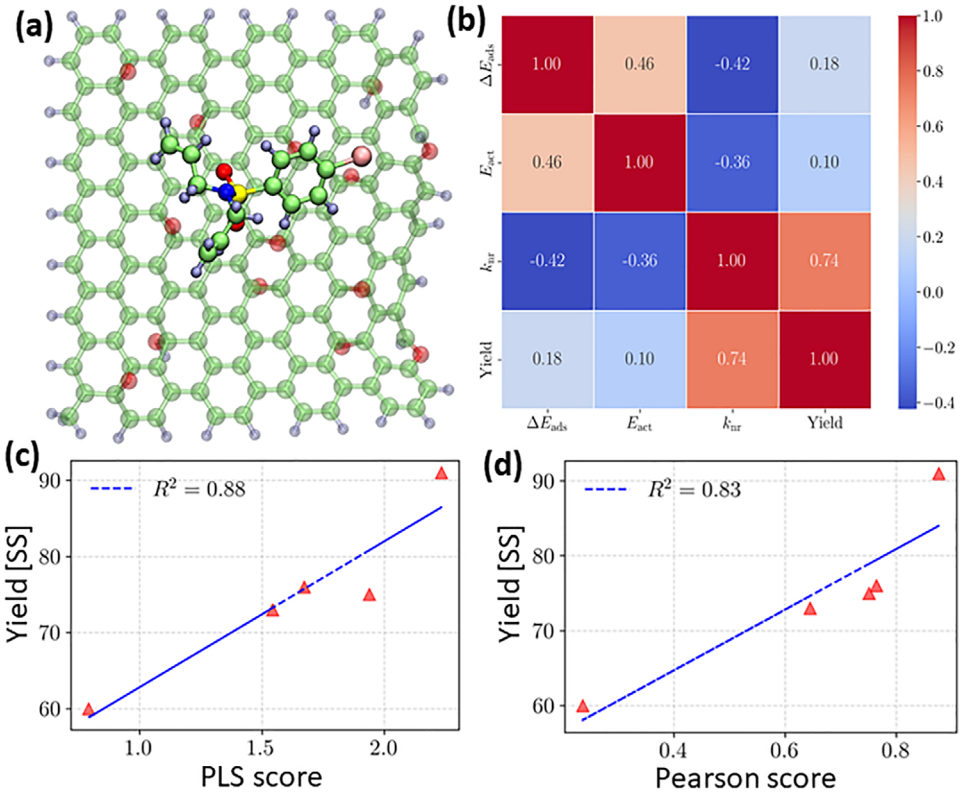

FIGURE 2 | (a) Compound 1a–1e adsorbed on a graphene sheet, as used in the simulations (ball-and-stick). Color scheme: carbon green; nitrogen blue; oxygen red; sulfur yellow; hydrogen light blue; halogens (F/Cl/Br/I) or CH_3 pink. (b) Correlation heatmap illustrating the relationships among (k_{nr}), adsorption energy (ΔE_{ads}), reaction barrier (E_{act}), and catalytic yield for halogen-substituted compounds. (c,d) Correlation of (a) PLS VIP scores and (b) Pearson scores with experimental yield under simulated solar irradiation. $k_{nr,}$ nonradiative relaxation rate; PLS, partial least squares; VIP, variable importance in projection.

vibrational modes, GO efficiently channels electronic excitations into vibrational heat, thereby driving the catalytic activity. Among the studied complexes, 1c displayed the highest k_{nr} (4.53×10^8 s^{-1}), closely followed by 1a (4.31×10^8 s^{-1}), while the lowest was observed for 1b (3.43×10^8 s^{-1}). Notably, k_{nr} values did not directly track product yields, indicating that nonradiative relaxation, though dominant, was not the sole governing factor. Taken together, the experimental yields under simulated solar irradiation are governed by the interplay between ΔE_{ads}, E_{act}, and k_{nr} (Table S1). The correlation analysis (Figure 2b) revealed that nonradiative relaxation contributes the largest weight (~74%), followed by adsorption energy (~18%) and activation barrier (~10%). A modest negative correlation (around −0.40) is observed between $\Delta E_{ads}/E_{act}$ and k_{nr}, suggesting that adsorption strength and barrier height tend to diminish as k_{nr} increases.

To further quantify descriptor importance, we applied two independent approaches: (i) Pearson correlation coefficients and (ii) Partial Least Squares (PLS) regression with Variable Importance in Projection (VIP) scores [39]. Both methods consistently identified k_{nr} as the dominant predictor of reaction yield. Its high Pearson coefficient (~0.74) and VIP score (> 1.0) confirmed its central role. ΔE_{ads} exerted a moderate influence (Pearson ~0.18, VIP < 1.0), while E_{act} contributed minimally (Pearson ~0.10, VIP = 0.38). Regression analyses further validated this descriptor hierarchy, yielding strong predictive performance (Pearson R^2 = 0.83, PLS R^2 = 0.88; Table S2 and Figures 2c, d). Our analysis highlighted that no single descriptor—adsorption energy, activation barrier, or k_{nr}—was sufficient on its own to account for the observed reaction yields. Instead, the efficiency originated from the collective interplay of these factors, where adsorption governed surface residence time, the barrier dictated kinetic feasibility, and k_{nr} channelized absorbed energy into heat. Among them, however, k_{nr} emerged as the dominant contributor, while ΔE_{ads} and E_{act} played supporting roles in fine-tuning the overall reaction outcome.

To explore the application of this GO-mediated photothermal RCM, we treated compound 2a in the presence of different organelle homing moieties containing 4-bromo-1,8-naphthalic anhydride (A) and 4-bromo-1,8-naphthalimide derivatives (B and C) in the presence of $Pd(OAc)_2$ as the catalyst in a Heck coupling condition to afford compound 3a–3c (Figures 3a and S24-S34). We designed compound 3a–3c to home into ER, mitochondria, and GA through 4-methyl-benzenesulfonamide, positively charged triphenylphosphonium cation and phenylsulfonamide moieties, respectively. We characterized compound 3a–c by UV–Vis and fluorescence spectroscopy, which revealed that all the compounds absorbed at λ_{max} = 360–375 nm and when excited at λ_{ex} = 360–375 nm light, all the compounds emitted at λ_{em} = 460–520 nm (Figure S35), capable of bioimaging.

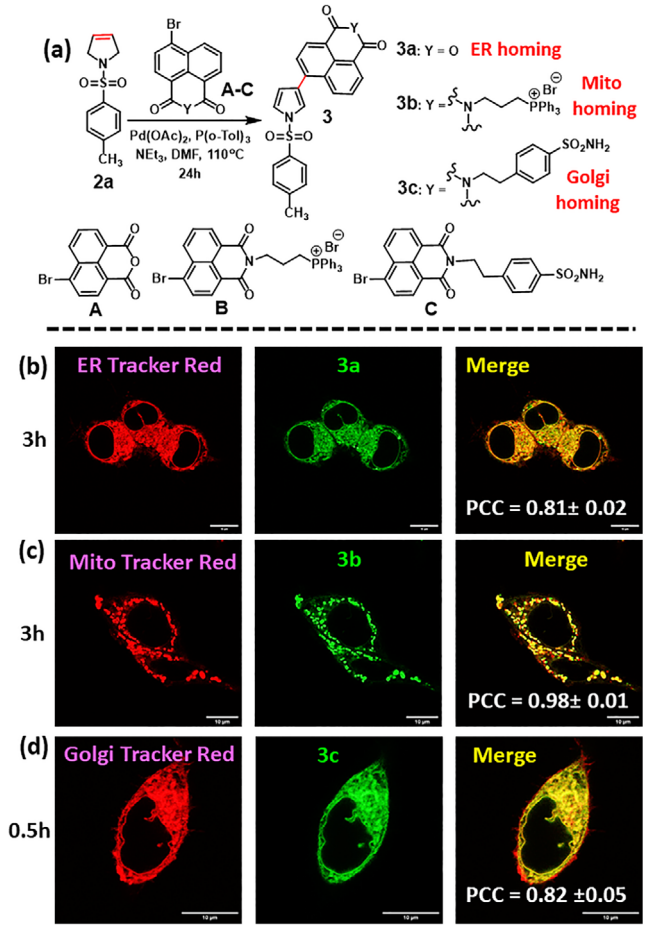

FIGURE 3 | (a) Synthetic scheme of the organelle-targeted fluorophores (3a-3c). (b-d) Confocal microscopy images of HCT-116 cells treated with 3a–3c (3a: 10 μM; 3b: 2.5 μM and 3c: 10 μM) for 3 h followed by staining the ER, mitochondria, and GA by ER Tracker Red, MitoTracker Red, and Golgi Tracker Red dyes, respectively. Scale bar = 10 μm. ER, endoplasmic reticulum; GA; Golgi apparatus.

For bioimaging, the fluorescence probe should be nontoxic to the cells. Hence, we evaluated the toxicity of compound 3a-c in HCT-116 colon cancer cells. We treated HCT-116 cells with compound 3a-c in a dose-dependent manner for 24 h followed by assessing the cell viability by MTT assay. From the MTT assay, it was clear that compound 3a–c showed IC_{50} = 20, 5, and more than 30 μM, respectively (Figure S36). We further evaluated the respective organelle imaging capability of 3a–c in HCT-116 cells. We treated HCT-116 cells with compound 3a,b (3a: 10 μM, 3b: 2.5 μM) separately for 3h and stained the ER and mitochondria with ER Tracker Red and MitoTracker Red dyes, followed by visualizing the live cells under confocal microscopy. From the confocal images, it was evident that 3a and 3b homed into ER and mitochondria efficiently, yielding merged yellow fluorescent signals with Pearson's correlation coefficients (PCC) = 0.81± 0.02 and 0.98±0.01 (n = 30), respectively (Figures 3b, c, and S37). On the other hand, we treated HCT-116 cells with compound 3c (10 μM) in a time-dependent manner for 0.5, 1, and 3h, stained the GA with GA Tracker Red dye, and visualized the cells under confocal microscopy. The confocal images demonstrated that compound 3c localized into the GA efficiently within 30 min and remained there for 3h with PCC = 0.82 ± 0.05, 0.81± 0.03, and 0.65 ± 0.02 (n = 30) at 0.5, 1 and 3h, respectively (Figures 3d and S38). We anticipate moderate homing of 3c in GA after 3h due to the back transport of proteins and lipids from GA into the ER in a time-dependent manner. [40, 41] These confocal images clearly confirmed that 3a,b homed efficiently into the ER and mitochondria within 3h and compound 3c efficiently homed into the GA within 30 min in HCT-116 cells.

3 | Conclusions

In conclusion, we have presented an efficient and high-yielding GO-mediated photothermal RCM using 940 nm LED, solar simulator, and natural sunlight with short reaction time with excellent GO recyclability. Theoretical calculations revealed that the photothermal RCM efficiency emerged from the collective interplay between substrate-GO absorption energy, activation barrier, and k_{nr}, which appeared as the dominating contributor for the overall outcome. The dihydropyrroles generated from this unique photothermal RCM can be further functionalized into diverse fluorescence probes for imaging ER, mitochondria, and GA in HCT-116 colon cancer cells. To the best of our knowledge, this is the first example of GO-mediated photothermal RCM in a sustainable manner, which has the potential to synthesize numerous complex organic molecules rapidly with high yield for biomedical applications.

Acknowledgments

SB sincerely thanks IIT Gandhinagar, Gujarat Council on Science and Technology (GUJCOST/STI/R&D/2020-21/1302) and Science and Engineering Research Board (CRG/2020/001127) for financial support. Preeti and TM acknowledge IIT Gandhinagar for the doctoral fellowship. RS and AM gratefully acknowledge the Indian Institute of Technology Gandhinagar, India, for providing research facilities and financial support. We thank PARAM Ananta for computational resources.

Conflicts of Interest

The authors declare no conflicts of interest.

References

1. L. H. Kugelmass, C. Tagnon, and E. E. Stach, "Photothermal Mediated Chemical Recycling to Monomers via Carbon Quantum Dotse," *Journal of the American Chemical Society* 145 (2023): 16090–16097, https://doi.org/10.1021/jacs.3c04448.

2. Y. Liu, Q. Zhong, P. Xu, et al., "Solar Thermal Catalysis for Sustainable and Efficient Polyester Upcycling," *Matter* 5 (2022): 1305.

3. Y. Miao, Y. Zhao, G. I. N. Waterhouse, R. Shi, L. I.-Z. Wu, and T. Zhang, "Photothermal Recycling of Waste Polyolefin Plastics Into Liquid Fuels With High Selectivity Under Solvent-Free Conditions," *Nature Communications* 14 (2023): 4242, https://doi.org/10.1038/s41467-023-40005-6.

4. X. Lou, X. Gao, Y. U. Liu, et al., "Highly Efficient Photothermal Catalytic Upcycling of Polyethylene Terephthalate via Boosted Localized Heating," *Chinese Journal of Catalysis* 49 (2023): 113–122, https://doi.org/10.1016/S1872-2067(23)64435-3.

5. C. Xing, H. Cai, D. Kang, and W. Sun, "Photothermal Catalysis: An Emerging Green Approach to Upcycling Plastic Waste," *Advanced Energy and Sustainability Research* 4 (2023): 2300015, https://doi.org/10.1002/aesr.202300015.

6. Y. U. Liu, X. Wang, Q. Li, et al., "Photothermal Catalytic Polyester Upcycling Over Cobalt Single-Site Catalyst," *Advanced Functional Materials* 33 (2023): 2210283, https://doi.org/10.1002/adfm.202210283.

7. J. Ma, N. Li, J. Wang, Z. Liu, Y. Han, and Y. Zeng, "In Vivo Synergistic Tumor Therapies Based on Copper Sulfide Photothermal Therapeutic Nanoplatforms," *Exploration* 3 (2023): 20220161.

8. M. Zhang, S. Ran, X. Yin, et al., "Mesoporous Polydopamine Nanoplatforms Loaded with Calcium Ascorbate for Amplified Oxidation and Photothermal Combination Cancer Therapy," *BMEMat* 1 (2023): e12041.

9. N. A. Romero and D. A. Nicewicz, "Organic Photoredox Catalysis," *Chemical Reviews* 116 (2016): 10075–10166, https://doi.org/10.1021/acs.chemrev.6b00057.

10. X. Yang and D. Wang, "Photocatalysis: From Fundamental Principles to Materials and Applications," *ACS Applied Energy Materials* 1 (2018): 6657–6693, https://doi.org/10.1021/acsaem.8b01345.

11. D. Staveness, I. Bosque, and C. R. J. Stephenson, "Free Radical Chemistry Enabled by Visible Light-Induced Electron Transfer," *Accounts of Chemical Research* 49 (2016): 2295–2306, https://doi.org/10.1021/acs.accounts.6b00270.

12. J. Twilton, C. Le, P. Zhang, M. H. Shaw, R. W. Evans, and D. W. C. Macmillan, "The Merger of Transition Metal and Photocatalysis," *Nature Reviews Chemistry* 1 (2017): 0052, https://doi.org/10.1038/s41570-017-0052.

13. F. He, W. Jeon, and W. Choi, "Photocatalytic Air Purification Mimicking the Self-Cleaning Process of the Atmosphere," *Nature Communications* 12 (2021): 2528.

14. X. I. Chen, Y. Chen, M. Yan, and M. Qiu, "Nanosecond Photothermal Effects in Plasmonic Nanostructures," *ACS Nano* 6 (2012): 2550–2557, https://doi.org/10.1021/nn2050032.

15. A. D. Phan, D. O. T. Nga, and N. A. Viet, "Theoretical Model for Plasmonic Photothermal Response of Gold Nanostructures Solutions," *Optics Communication* 410 (2018): 108–111, https://doi.org/10.1016/j.optcom.2017.10.008.

16. H. Yu, Y. Peng, Y. Yang, and Z.-Y. Li, "Plasmon-Enhanced Light–Matter Interactions and Applications," *npj Computational Materials* 5 (2019): 45.

17. J. A. Schuller, E. S. Barnard, W. Cai, Y. C. Jun, J. S. White, and M. L. Brongersma, "Plasmonics for Extreme Light Concentration and Manipulation," *Nature Materials* 9 (2010): 193–204, https://doi.org/10.1038/nmat2630.

18. R. K. Kashyap, S. Tyagi, and P. P. Pillai, "Plasmon Enabled Claisen Rearrangement With Sunlight," *Chemical Communications* 59 (2023): 13293–13296, https://doi.org/10.1039/D3CC04278B.

19. N. S. Abadeer and C. J. Murphy, "Recent Progress in Cancer Thermal Therapy Using Gold Nanoparticles," *Journal of Physical Chemistry C* 120 (2016): 4691–4716, https://doi.org/10.1021/acs.jpcc.5b11232.

20. N. Lemcoff, N. B. Nechmad, O. R. Eivgi, et al., "Plasmonic Visible–Near Infrared Photothermal Activation of Olefin Metathesis Enabling Photoresponsive Materials," *Nature Chemistry* 15 (2023): 475–482, https://doi.org/10.1038/s41557-022-01124-7.

21. I. Ibrahim, D. H. Seo, A. M. McDonagh, H. K. Shon, and L. Tijing, "Semiconductor Photothermal Materials Enabling Efficient Solar Steam Generation Toward Desalination and Wastewater Treatment," *Desalination* 500 (2021): 114853.

22. L. Zhu, M. Gao, C. K. N. Peh, and G. W. Ho, "Solar-driven Photothermal Nanostructured Materials Designs and Prerequisites for Evaporation and Catalysis Applications," *Mater Horiz* 5 (2018): 323–343, https://doi.org/10.1039/C7MH01064H.

23. H. Wang, A. I. Du, X. Ji, et al., "Enhanced Photothermal Conversion by Hot-Electron Effect in Ultrablack Carbon Aerogel for Solar Steam Generation," *ACS Applied Materials and Interfaces* 11 (2019): 42057–42065, https://doi.org/10.1021/acsami.9b12918.

24. K. Qi, B. Sun, S.-Y. Liu, and M. Zhang, "Research Progress on Carbon Materials in Tumor Photothermal Therapy," *Biomedicine & Pharmacotherapy* 165 (2023): 115070, https://doi.org/10.1016/j.biopha.2023.115070.

25. J. Lu, Y. Shi, Z. Chen, et al., "Photothermal Effect of Carbon Dots for Boosted Photothermal-Assisted Photocatalytic Water/Seawater Splitting Into Hydrogen," *Chemical Engineering Journal* 453 (2023): 139834, https://doi.org/10.1016/j.cej.2022.139834.

26. Y. Wang, H.-M. Meng, G. Song, Z. Li, and X.-B. Zhang, "Conjugated-Polymer-Based Nanomaterials for Photothermal Therapy," *ACS Applied Polymer Materials* 2 (2020): 4258–4272, https://doi.org/10.1021/acsapm.0c00680.

27. D. Xu, Z. Li, L. Li, and J. Wang, "Insights Into the Photothermal Conversion of 2D MXene Nanomaterials: Synthesis, Mechanism, and Applications," *Advanced Functional Materials* 30 (2020): 2000712, https://doi.org/10.1002/adfm.202000712.

28. M. E. Matter, C. Tagnon, and E. E. Stache, "Recent Applications of Photothermal Conversion in Organic Synthesis," *ACS Central Science* 10 (2024): 1460–1472, https://doi.org/10.1021/acscentsci.4c00545.

29. M. E. Matter, L. Camdzic, and E. E. Stache, "Photothermal Conversion by Carbon Black Facilitates Aryl Migration by Photon-Promoted Temperature Gradients," *Angewandte Chemie International Edition* 62 (2023): e202308648, https://doi.org/10.1002/anie.202308648.

30. S. Oh, H. Jiang, L. H. Kugelmass, and E. E. Stache, "Recycling of Post-Consumer Waste Polystyrene Using Commercial Plastic Additives," *ACS Central Science* 11 (2024): 57–65, https://doi.org/10.1021/acscentsci.4c01317.

31. K. Yang, S. Zhang, G. Zhang, X. Sun, S.-T. Lee, and Z. Liu, "Graphene in Mice: Ultrahigh in Vivo Tumor Uptake and Efficient Photothermal Therapy," *Nano Letters* 10 (2010): 3318–3323, https://doi.org/10.1021/nl100996u.

32. J. T. Robinson, S. M. Tabakman, Y. Liang, et al., "Ultrasmall Reduced Graphene Oxide With High Near-Infrared Absorbance for Photothermal Therapy," *Journal of the American Chemical Society* 133 (2011): 6825–6831, https://doi.org/10.1021/ja2010175.

33. S. Liu, X. Pan, and H. Liu, "Two-Dimensional Nanomaterials for Photothermal Therapy," *Angewandte Chemie International Edition* 59 (2020): 5890–5900, https://doi.org/10.1002/anie.201911477.

34. K. C. Nicolaou, P. G. Bulger, and D. Sarlah, "Metathesis Reactions in Total Synthesis," *Angewandte Chemie International Edition* 44 (2005): 4490–4527, https://doi.org/10.1002/anie.200500369.

35. M. Yu, S. Lou, and F. Gonzalez-Bobes, "Ring-Closing Metathesis in Pharmaceutical Development: Fundamentals, Applications, and Future Directions," *Organic Process Research & Development* 22 (2018): 918–946, https://doi.org/10.1021/acs.oprd.8b00093.

36. S. J. Connon, M. Rivard, M. Zaja, and S. Blechert, "Practical Olefin Metathesis in Protic Media Under an Air Atmosphere," *Advanced Synthesis & Catalysis* 345 (2003): 572–575, https://doi.org/10.1002/adsc.200202201.

37. F. Neese, "The ORCA Program System," *WIREs Computational Molecular Science* 2 (2012): 73–78, https://doi.org/10.1002/wcms.81.

38. F. Neese, "Software Update: The ORCA Program System—Version 6.0," *WIREs Computational Molecular Science* 15 (2025): e70019, https://doi.org/10.1002/wcms.70019.

39. B. Mahieu, E. L. M. Qannari, and B. Jaillais, "Extension and Significance Testing of Variable Importance in Projection (VIP) Indices in Partial Least Squares Regression and Principal Components Analysis," *Chemometrics and Intelligent Laboratory Systems* 242 (2023): 104986, https://doi.org/10.1016/j.chemolab.2023.104986.

40. D. Wlodkowic, J. Skommer, D. Mcguinness, C. Hillier, and Z. Darzynkiewicz, "ER–Golgi Network—A Future Target for Anti-cancer Therapy," *Leukemia Research* 33 (2009): 1440–1447, https://doi.org/10.1016/j.leukres.2009.05.025.

41. A. Spang, "Retrograde Traffic from the Golgi to the Endoplasmic Reticulum," *Cold Spring Harbor perspectives in biology* 5 (2013): a013391, https://doi.org/10.1101/cshperspect.a013391.

Supporting Information

Additional supporting information can be found online in the Supporting Information section.

Supporting File 1: General procedure for GO-mediated photothermal RCM: In a round bottle flask, compound 1a–1j (1 eq., 0.198 mmol) and the substrate were dissolved in DMF:H_2O (1:3, v/v, total volume 2 mL), and GO (1.5 mg) was added to the solution in a sealed reaction vial. Subsequently, 3 mol% of Grubbs' second-generation catalyst (0.03 eq., 5.06 mg) was added. The reaction mixture was irradiated with a 940 nm LED for 10 min. The reaction temperature was maintained at approximately 44–46 °C due to photothermal heating by GO. Completion of the reaction was monitored through thin-layer chromatography (TLC). Upon completion, the reaction mixture was cooled to room temperature, centrifuged the reaction mixture at 500 RPM for 5 min to collect the GO for future use, then workup with ice-cold water and ethyl acetate. The solvent was evaporated on the rotary evaporator, and the reaction mixture was purified with 100–200 mesh silica in 20% Ethyl acetate in hexane. The authors have cited additional references within the Supporting Information [42–47].